Optica Applicata, Vol. LIII, No. 1, 2023
DOI: 10.37190/oa230109

Phase retrieval without phase unwrapping for white blood cells in deep-learning phase-shifting digital holography

Shuyang Jin[1], Xiaoqing Xu[2,*], Jili Chen[2], Yudan Ni[2]

[1]Centre of Information Technology, Changzhou Vocational Institute of Mechatronic Technology, Changzhou 213164, Jiangsu, China

[2]Institute of Mold Technology, Changzhou Vocational Institute of Mechatronic Technology, Changzhou 213164, Jiangsu, China

[*]Corresponding author: xxqyzzd@sina.com

Phase retrieval and phase unwrapping are the two important problems for enabling quantitative phase imaging of cells in phase-shifting digital holography. To simultaneously cope with these two problems, a deep-learning phase-shifting digital holography method is proposed in this paper. The proposed method can establish the continuous mapping function of the interferogram to the ground-truth phase using the end-to-end convolutional neural network. With a well-trained deep convolutional neural network, this method can retrieve the phase from one-frame blindly phase -shifted interferogram, without phase unwrapping. The feasibility and applicability of the proposed method are verified by the simulation experiments of the microsphere and white blood cells, respectively. This method will pave the way to the quantitative phase imaging of biological cells with complex substructures.

Keywords: digital holography, phase retrieval, deep learning.

1. Introduction

Phase-shifting digital holography (PSDH) [1–4] has been widely used in many fields of engineering and biology owing to the advantages of its label-free, non-contact, high sensitivity and high resolution. In PSDH, phase retrieval and phase unwrapping are the two equally important issues for realizing quantitative phase imaging (QPI) of cells [5].

Traditionally, the problem of phase extraction is solved by using various phase demodulation methods, such as the two-step Gram–Schmidt orthonormalization method [6], four-step phase-shifting (FSPS) algorithm [7], advanced iterative algorithm (AIA) [8] and so on. Though these algorithms are satisfactory methods for phase retrieval, the prior knowledge of phase-shifting interferogams is emphasized and then

suitable algorithms aimed to different imaging objects are presented, leading to these algorithms without universality. In addition, the retrieved phase value using the arctangent function is often wrapped in the limited range of $(-\pi, \pi)$ [9] because an optical path difference is greater than the probe wavelength, resulting in the phase ambiguity. To address this issue, different types of phase unwrapping algorithms are proposed to obtain the true phase. However, the phase unwrapping procedure is often complex and time-consuming, and it cannot work well when the object is high-aspect-ratio sample [10, 11]. Another crucial method for addressing the problem of wrapped phase is the dual-wavelength PSDH technique [2, 12–14]. Using this method, the unwrapped phase at the longer synthetic wavelength can be obtained by subtraction operation between two wrapped phases of single wavelength, expanding the measured range of the imaging object; the phase at the shorter synthetic wavelength can be achieved by addition operation between the wrapped phases at each wavelength, improving the accuracy of phase imaging. However, dual-wavelength PSDH requires the dual-phase demodulation and increases the complexity of recording and coping with phase-shifting interferograms, compared with single-wavelength PSDH.

More recently, deep learning (DL) has attracted researcher's attention due to the fact that deep convolutional neural network (DCNN) has the capability of establishing the end-to-end mapping relation in the pixel-level. If there are sufficient number of neural network fitting parameters in the DCNN, DL can theoretically approximate any continuous functions [15]. With the increasing of computing power, DL has emerged as a rapidly developing technique [16] and has been shown to be useful in optical image reconstruction and digital holography, such as the phase aberration automatic compensation [17], autofocusing holographic imaging [18], particle volume reconstruction [19], fast off-axis holographic phase retrieval [20], phase recovery and image reconstruction [21], in-line digital holographic reconstruction [22], phase unwrapping [23], dual -wavelength interferogram decoupling [24], and interferogram denoising [25]. Though trained DCNN-based methods can obtain the state-of-the-art performance of phase image reconstruction and digital holographic imaging, they either require big datasets or indirectly obtain the phase information.

Here, in this paper, to simultaneously address the two problems of phase retrieval and phase unwrapping, we propose a new deep-learning phase-shifting digital holography (DLPSDH) method based on a DCNN, to establish the continuous mapping function relation of the interferogram to the phase. The proposed method trained in an end-to-end fashion on the minimum number of datasets, only requires one-frame randomly phase-shifted interferogram as input, and then directly outputs the phase information, without phase unwrapping. This method has better phase retrieval accuracy, compared with other traditional phase demodulation methods. The algorithm description of the DLPSDH method is introduced, and then its feasibility and applicability are demonstrated by the simulation experiments of the microsphere and white blood cells (WBCs), respectively.

2. Algorithm descriptions

2.1. Phase retrieval inverse problem

In PSDH, the intensity of the k-th phase-shifted interferogram can be defined by

$$I_k(x, y) = a(x, y) + b(x, y)\cos\left[\varphi(x, y) + \delta_k\right], \quad k = 0, 1, 2, ..., K \tag{1}$$

where $a(x, y)$, $b(x, y)$, $\varphi(x, y)$ and δ_k represent the background intensity, the modulation amplitude, the measured phase and the phase shifts, respectively.

Phase retrieval is a highly ill-posed problem since depending on intensity-only measurements. Typically, the phase can be retrieved from multiple phase-shifted interferograms by using the traditional phase demodulation methods. However, here, the phase retrieved from single interferogram with the DLPSDH method based on a well -trained DCNN, as shown in Fig. 1, can be expressed as

$$\varphi_k^* = \xi\{I_k; \Theta\} \tag{2}$$

where $\xi(\cdot)$ represents the continuous mapping function of the interferogram I_k to the extracted phase φ_k^* and Θ is the neural network fitting parameters.

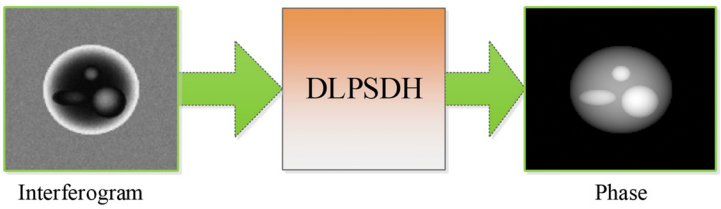

Fig. 1. Schematic of the proposed DLPSDH method.

Subsequently, the estimate function $\xi(\cdot)$ can be achieved by solving

$$f\{\Theta\} = \frac{1}{\Gamma}\sum_{k=1}^{\Gamma}\left\|\varphi_k - \xi_{\psi \in \Theta}(I_k; \Theta)\right\|_2^2 \tag{3}$$

where $f\{\Theta\}$ is the loss function in our DCNN and Γ is the batch size. Once the loss function $f\{\Theta\}$ is minimized, the continuous mapping function $\xi(\cdot)$ in Eq. (3) can be obtained to extract the phase from single interferogram, without phase unwrapping.

2.2. Encoder–decoder architecture

In our study, we adopt U-Net [26] to construct an encoder–decoder network structure, as presented in Fig. 2, which is composed of a contracting path and an expansive path in the left and right sides, respectively.

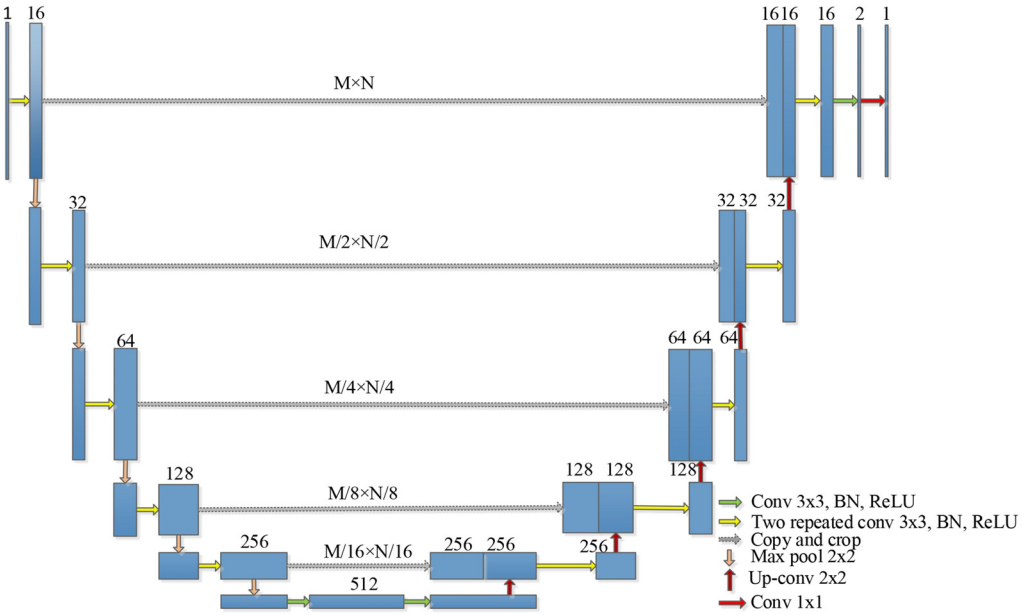

Fig. 2. Detailed network architecture of the proposed DLPSDH method.

The input of the proposed DCNN is the interferogram, and the output of the proposed DCNN is the phase image. The contracting path in the DLPSDH method, which is essentially encoding process, consists of the repeated application of two 3×3 convolutions, each followed by a batch normalization (BN) and a rectified linear unit (ReLU), and a 2×2 max pooling operation with stride 2 for down-sampling. Specifically, let z_j^{ℓ} denote the input interferogram data of the ℓ-th convolutional layer, which can be expressed as

$$\xi^{\ell}(z_j^{\ell}) = \mathrm{ReLU}\left\{ \mathrm{BN}\left[\sum_{i=1}^{N^{(\ell-1)}} z_i^{(\ell-1)} \otimes W_{ij}^{\ell} + B_j^{\ell} \right] \right\}, \quad j = 1, 2, ..., N^{(\ell)} \tag{4}$$

where W, B, $\otimes$ and $N^{(\ell)}$ respectively denote the weight, the bias, the convolutional operation, and the number of the channels; $\xi^{\ell}(\cdot)$ is the function mapping of the ℓ-th convolutional layer. The BN in Eq. (4) can be expressed as

$$\hat{z}_j = \gamma \frac{z_j - \mu[z_j]}{\sqrt{\tau^2 + \varepsilon}} + \beta \tag{5}$$

where $\mu[z_j] = \dfrac{1}{N^{(\ell)}} \sum_{j=1}^{N^{(\ell)}} z_j$ and $\tau^2 = \dfrac{1}{N^{(\ell)}} \sum_{j=1}^{N^{(\ell)}} (z_j - \mu[z_j])^2$, and $\hat{z}_j$ is the output

of the BN layer, ε is a regularization parameter, γ is a scaling factor and β is the shifting factor. The ReLU activation function in Eq. (4) can be defined as

$$\mathrm{ReLU}(z_j) = \max(0, z_j) \tag{6}$$

With the function mapping each convolutional layer, the continuous mapping function $\xi\{\cdot\}$ can be expressed as

$$\xi\{\cdot\} = \sum_{i=1}^{A} \xi^i\{\cdot\} \tag{7}$$

where A is the number of the convolutional layers.

Without a loss of generality, take the interferogram size $M \times N$ pixels as an example for illustrating the process of the multichannel features extraction of the interferogram related to phase retrieval. At each down-sampling step, in the contracting path, we double the number of the channels, which then becomes 16, 32, 64, 128, 256 and 512, respectively; meanwhile, we, respectively, halve the size of the input interferogram, which becomes $M \times N$, $M/2 \times N/2$, $M/4 \times N/4$, $M/8 \times N/8$, $M/16 \times N/16$ and $M/32 \times N/32$ pixels. The expansive path in the DLPSDH method, which is virtually decoding process, consists of a 2×2 deconvolution concatenating with correspondingly copied feature map in the contracting path, and two 3×3 convolutions, each followed by a BN and ReLU. At each up-sampling step, we halve the number of the channels, which then becomes 512, 256, 128, 64, 32 and 16, and we simultaneously double the size of the output image, which becomes $M/32 \times N/32$, $M/16 \times N/16$, $M/8 \times N/8$, $M/4 \times N/4$, $M/2 \times N/2$ and $M \times N$ pixels, respectively, in the expansive path. Finally, the number of the channels and the size of the output phase image are respectively set as 1 and $M \times N$ pixels. It is worth noting that the proposed DCNN framework is composed of 24 convolutional and 5 deconvolutional operations. Additionally, in the process of encoding and decoding structure of the input interferogram by using the DLPSDH method, the structures related to the phase retrieval are retained while those structures, which are not associated with the phase retrieval, are discarded. The proposed DLPSDH method is actually a symmetric end-to-end network architecture for phase retrieval without phase unwrapping.

3. Numerical simulations

To demonstrate the proof-of-concept of the proposed DLPSDH method, the microsphere and WBCs are employed as the phase imaging objects. The quantitative phase $\varphi(x, y)$ of the homogeneous microsphere can be expressed as

$$\varphi(x, y) = \frac{4\pi(n_1 - n_m)}{\lambda} \sqrt{r^2 - x^2 - y^2} \tag{8}$$

where r denotes the radius of the homogeneous microsphere, λ is the wavelength, n_1 is the refractive index of the homogeneous microsphere. The leukocytes are mainly con-

sisted of the monocyte, lymphocyte, neutrophil, basophil and eosinophil. The monocyte is composed of the ellipsoidal cytoplasm and globular nucleus, and its quantitative phase $\varphi(x, y)$ can be defined by

$$\begin{aligned}\varphi(x, y) &= \frac{4\pi(n_2 - n_m)}{\lambda} c\sqrt{1 - \left(\frac{x}{a}\right)^2 - \left(\frac{y}{b}\right)^2} \\ &+ \frac{4\pi(n_1 - n_2)}{\lambda}\sqrt{r_1^2 - (x + \alpha_0)^2 - (y + \beta_0)^2}\end{aligned} \tag{9}$$

where a, b and c are the half axis lengths of the ellipsoidal cytoplasm along the x-, y- and z-axis directions, respectively; r_1 denotes the radius of the globular nucleus; n_1 and n_2 are the refractive indices of the globular nucleus and ellipsoidal cytoplasm, respectively. The lymphocyte is composed of the globular cytoplasm and nucleus, and its quantitative phase $\varphi(x, y)$ can be expressed as

$$\begin{aligned}\varphi(x, y) &= \frac{4\pi(n_2 - n_m)}{\lambda}\sqrt{r_2^2 - x^2 - y^2} \\ &+ \frac{4\pi(n_1 - n_2)}{\lambda}\sqrt{r_1^2 - (x + \alpha_0)^2 - (y + \beta_0)^2}\end{aligned} \tag{10}$$

where r_1 and r_2 denote the radii of the globular nucleus and cytoplasm, n_1 and n_2 are the refractive indices of the globular nucleus and cytoplasm, respectively. The neutrophil is composed of globular cytoplasm, an ellipsoidal and two different globular nuclei, and its quantitative phase $\varphi(x, y)$ can be defined by

$$\begin{aligned}\varphi(x, y) &= \frac{4\pi(n_1 - n_4)}{\lambda}\sqrt{r_1^2 - (x + \alpha_0)^2 - (y + \beta_0)^2} \\ &+ \frac{4\pi(n_2 - n_4)}{\lambda} c\sqrt{1 - \left(\frac{x + \alpha_1}{a}\right)^2 - \left(\frac{y + \beta_1}{b}\right)^2} \\ &+ \frac{4\pi(n_3 - n_4)}{\lambda}\sqrt{r_3^2 - (x + \alpha_3)^2 - (y + \beta_3)^2} \\ &+ \frac{4\pi(n_4 - n_m)}{\lambda}\sqrt{r_4^2 - x^2 - y^2}\end{aligned} \tag{11}$$

where r_1, r_3 and r_4 are the radii of the two different globular nuclei and globular cytoplasm, respectively; a, b and c are the half axis lengths of the ellipsoidal nucleus along the x-, y- and z-axis directions, respectively; n_1, n_2, n_3 and n_4 denote the refractive indices of the globular nucleus, ellipsoidal nucleus, globular nucleus and globular cytoplasm, respectively. The basophil is composed of the globular nucleus, ellipsoidal nucleus and globular cytoplasm, and its quantitative phase $\varphi(x, y)$ can be expressed as

$$\varphi(x,y) = \frac{4\pi(n_1-n_3)}{\lambda}\sqrt{r_1^2-(x+\alpha_0)^2-(y+\beta_0)^2} + \frac{4\pi(n_2-n_3)}{\lambda}c\sqrt{1-\left(\frac{x+\alpha_1}{a}\right)^2-\left(\frac{y+\beta_1}{b}\right)^2} + \frac{4\pi(n_3-n_m)}{\lambda}\sqrt{r_3^2-x^2-y^2} \tag{12}$$

where r_1 and r_3 denote the radii of the globular nucleus and cytoplasm; a, b and c are the half axis lengths of the ellipsoidal nucleus along the x-, y- and z-axis directions, respectively; n_1, n_2 and n_3 represent the refractive indices of the globular nucleus, ellipsoidal nucleus and globular cytoplasm, respectively. The eosinophil is composed of two different ellipsoidal nuclei and a globular cytoplasm, and its quantitative phase $\varphi(x, y)$ can be defined by

$$\varphi(x,y) = \frac{4\pi(n_1-n_3)}{\lambda}c_1\sqrt{1-\left(\frac{x+\alpha_0}{a_1}\right)^2-\left(\frac{y+\beta_0}{b_1}\right)^2} + \frac{4\pi(n_2-n_3)}{\lambda}c_2\sqrt{1-\left(\frac{x+\alpha_1}{a_2}\right)^2-\left(\frac{y+\beta_1}{b_2}\right)^2} + \frac{4\pi(n_3-n_m)}{\lambda}\sqrt{r_3^2-x^2-y^2} \tag{13}$$

where r_3 denotes the radius of the globular cytoplasm; a_1, a_2, b_1, b_2, c_1 and c_2 are the half axis lengths of the ellipsoidal nucleus along the x-, y- and z-axis directions, respectively; n_1, n_2 and n_3 are the refractive indices of the two different ellipsoidal nuclei and the globular cytoplasm, respectively. Note that n_m represents the refractive index of the surrounding medium; α_0, α_1, β_0 and β_1 denote the central distances between the cytoplasm and nucleus along the x- and y-axis directions, respectively.

For homogeneous microsphere and WBCs, a series of phase-shifted interferograms with a size of 128 × 128 pixels and ground-truth phases are generated according to Eq. (1) and Eqs. (8)–(13) by setting the parameters as follows:

– the phase shift δ is a random phase shift in the range from 0 to 3π;

– for the microsphere, the background intensity is $a(x, y) = 100\exp[-0.015(x^2 + y^2)]$, and the modulation amplitude is $b(x, y) = 90\exp[-0.015(x^2 + y^2)]$;

– for the WBCs, the background intensity is $a(x, y) = 60\exp[-0.02(x^2 + y^2)]$, and the modulation amplitude is $b(x, y) = 50\exp[-0.02(x^2 + y^2)]$;

– for the WBCs, zero-mean Gaussian noise with standard deviation $\sigma = 1$ is added to each phase-shifted interferogram;

– for the microsphere, $\lambda = 532$ nm, $r = 4$ μm, $n_1 = 1.4$, $n_m = 1.3$;

– for the monocyte, $r_1 = 3.4$ μm, $\alpha_0 = 0$, $\beta_0 = 2$ μm, $n_1 = 1.44$, $a = 6$ μm, $b = 6.5$ μm, $c = 10$ μm, $n_2 = 1.37$;

– for the lymphocyte, $r_1 = 2$ μm, $n_1 = 1.45$, $\alpha_0 = -1$ μm, $\beta_0 = -2$ μm, $r_2 = 5$ μm, $n_2 = 1.38$;

– for the neutrophil, $r_1 = 1$ μm, $n_1 = 1.47$, $\alpha_0 = 0$, $\beta_0 = 2$ μm, $a = 2$ μm, $b = 1$ μm, $c = 1$ μm, $n_2 = 1.45$, $\alpha_1 = 2.5$ μm, $\beta_1 = -1$ μm, $r_3 = 2$ μm, $n_3 = 1.43$, $\alpha_3 = -2$ μm, $\beta_3 = -1.5$ μm, $r_4 = 5.5$ μm, $n_4 = 1.37$;

– for the basophil, $r_1 = 1$ μm, $n_1 = 1.47$, $\alpha_0 = 1.8$ μm, $\beta_0 = -1.5$ μm, $a = 1.5$ μm, $b = 1$ μm, $c = 1$ μm, $\alpha_1 = -1.8$ μm, $\beta_1 = -1$ μm, $n_2 = 1.45$, $r_3 = 5$ μm, $n_3 = 1.37$;

– for the eosinophil, $n_1 = 1.46$, $a_1 = 2$ μm, $b_1 = 1$ μm, $c_1 = 1$ μm, $\alpha_0 = -2.5$ μm, $\beta_0 = 1.5$ μm, $n_2 = 1.44$, $a_2 = 2$ μm, $b_2 = 1$ μm, $c_2 = 1$ μm, $\alpha_1 = -1$ μm, $\beta_1 = -1.5$ μm, $r_3 = 6$ μm, $n_3 = 1.37$;

– for the white blood cells, $\lambda = 632.8$ nm, $n_m = 1.33$.

Base on the parameters above, we construct the minimum number of datasets composed of 1200 randomly phase-shifted interferograms and their corresponding ground -truth phases for the homogeneous microsphere and inhomogeneous WBCs to test the proposed DLPSDH method. During training the DLPSDH method, the training epochs for the microsphere and WBCs are about 42; the batch size is 4; the learning rate is firstly set to be 0.1, and then it decays with a rate of 0.1 each 20 training epochs; the adaptive moment estimation (Adam) based optimizer [27] is employed to minimize the loss function in Eq. (3) by using iterative back-propagation algorithm.

4. Feasibility study

In order to verify the feasibility of the DLPSDH method, according to Eq. (8), the original phase of the homogeneous microsphere is shown in Fig. 3(a). Figure 3(c) presents

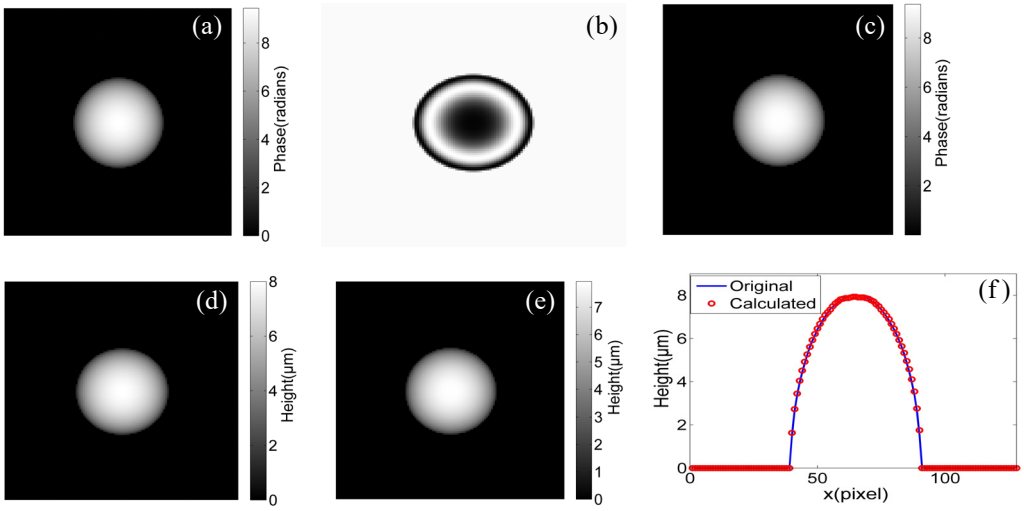

Fig. 3. The homogeneous microsphere: (a) the original phase, (b) one-frame interferogram with unknown phase shift, (c) the retrieved phase with the DLPSDH method, (d) the original height, (e) the calculated height, and (f) the central horizontal sections of (d) and (e).

the unwrapped phase extracted from one-frame interferograms with unknown phase shift, as shown Fig. 3(b), with the DLPSDH method. Note that the interferograms in the testing dataset are different from those in the training dataset. For comparison, the original height of the homogeneous microsphere is presented in Fig. 3(d). The calculated height of the homogeneous microsphere, as shown in Fig. 3(e), can be obtained from Fig. 3(c) by

$$h = \frac{\varphi \lambda}{2\pi(n_1 - n_m)} \tag{14}$$

To test the performance of the DLPSDH method, the central horizontal sections of the original and calculated heights of the homogeneous microsphere in the central horizontal row are depicted in Fig. 3(f). As can be seen from Fig. 3(f), the calculated height curve (circle) almost agrees with the original height curve (solid line). Through the analysis and calculation, the measuring maximum height of the microsphere is 7.9373 μm. Compared with the original value, that is 8 μm, the error is 0.78%. The result shows that the DLPSDH method is feasible to retrieve the unwrapped phase from one -frame phase-shifted interferogram.

5. Phase imaging for cells with substructures

Although WBCs originated from different precursor cells have different substructures, they play an important role in immune defense in humans. Since WBCs are optically transparent phase objects, QPI of WBCs has become a very popular field of study.

To demonstrate the applicability of the proposed method, we firstly present the original phase of the monocyte cell according to Eq. (9), as shown in Fig. 4(a). It can be seen from Fig. 4(a) that the monocyte cell has the globular nucleus. One-frame interferograms with 1 rad phase shift, as presented in Fig. 4(b), are employed to extract the phase of the monocyte cell, as shown in Fig. 4(c), using the DLPSDH method. To compare the measuring accuracy, the phases obtained with the AIA and FSPS methods are respectively presented in Figs. 4(d) and (e). In the AIA method, 4-frame randomly phase-shifted interferograms are used to retrieve the phase of the monocyte cell. In the FSPS algorithm, the phase of the monocyte cell is extracted from 4-frame interferograms with 0, π/2, π and 3π/2 known phase shifts. It is worthy to note that both the AIA and FSPS methods require the additional phase unwrapping operation, compared with the DLPSDH method; moreover, the FSPS method needs known phase shifts. Here, we introduce the root of mean square error (RMSE), which can be described by

$$\mathrm{RMSE} = \sqrt{\frac{1}{MN}\sum_{i=1}^{M}\sum_{j=1}^{N}(\varphi'_{ij} - \varphi_{ij})^2} \tag{15}$$

where φ'_{ij} and φ_{ij} are the retrieved and original phases, respectively. Through the calculation, the root mean square errors (RMSEs) of the monocyte cell with the proposed

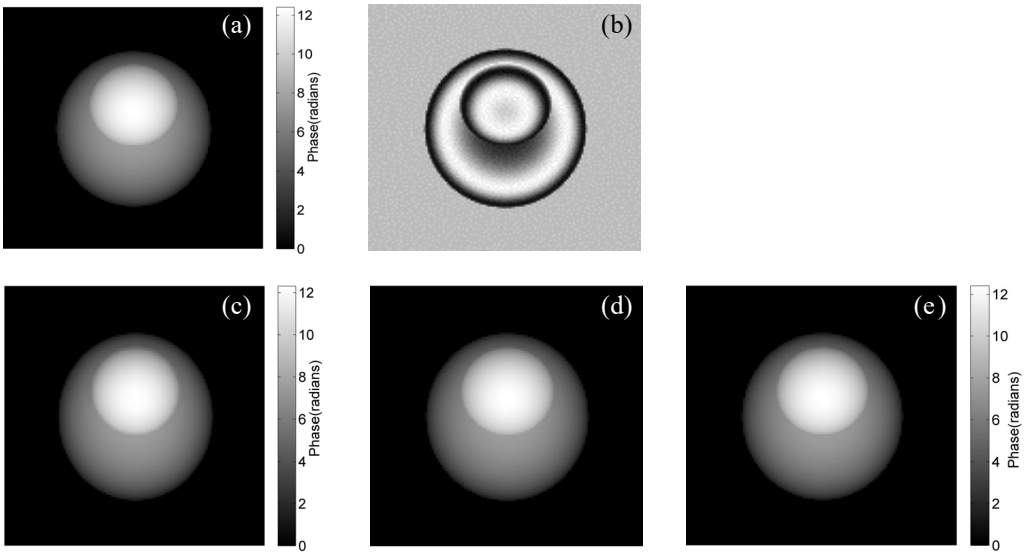

Fig. 4. The monocyte cell: (a) the original phase, (b) one-frame interferogram, (c), (d) and (e) the extracted phases with the DLPSDH, AIA and FSPS methods, respectively.

method, AIA and FSPS methods, respectively, are 0.053, 0.078 and 0.079 rad. Obviously, it can be seen that the accuracy of the phase extraction with the proposed method is higher than those with the AIA or FSPS methods, showing the applicability of the proposed method.

Secondly, we present the original phase of the neutrophil cell according to Eq. (11), as shown in Fig. 5(a), and its interferogram with 5 rad phase shift is shown in Fig. 5(b). It can be clearly seen from Fig. 5(a) that the neutrophil cell has the globular cytoplasm, an ellipsoidal and two globular nuclei. For the neutrophil cell, to investigate the performance of the DLPSDH method in the presence of noise, Gaussian noise with zero -mean and different standard deviations σ are added to a set of randomly phase-shifted interferograms. Here, we introduce the peak signal-to-noise ratio (PSNR) and structural similarity index measure (SSIM) [28], which can be respectively expressed as

$$\mathrm{PSNR} = 10\log_{10}\frac{(2^t-1)^2}{\frac{1}{MN}\sum_{i=1}^{M}\sum_{j=1}^{N}\left[\varphi_1(i,j)-\varphi_2(i,j)\right]^2} \tag{16}$$

$$\mathrm{SSIM} = \frac{(2\mu_1\mu_2+c_1)(2\tau_{1,2}+c_2)}{(\mu_1^2+\mu_2^2+c_1)(\tau_1^2+\tau_2^2+c_2)} \tag{17}$$

where φ_1 is the true phase image, and φ_2 is the extracted phase with different algorithms; t is set as 8; μ_1, τ_1, μ_2 and τ_2 are, respectively, the mean and standard deviation of the φ_1 and φ_2 phase images; $\tau_{1,2}$ is the cross variance of φ_1 and φ_2; c_1 and c_2 are

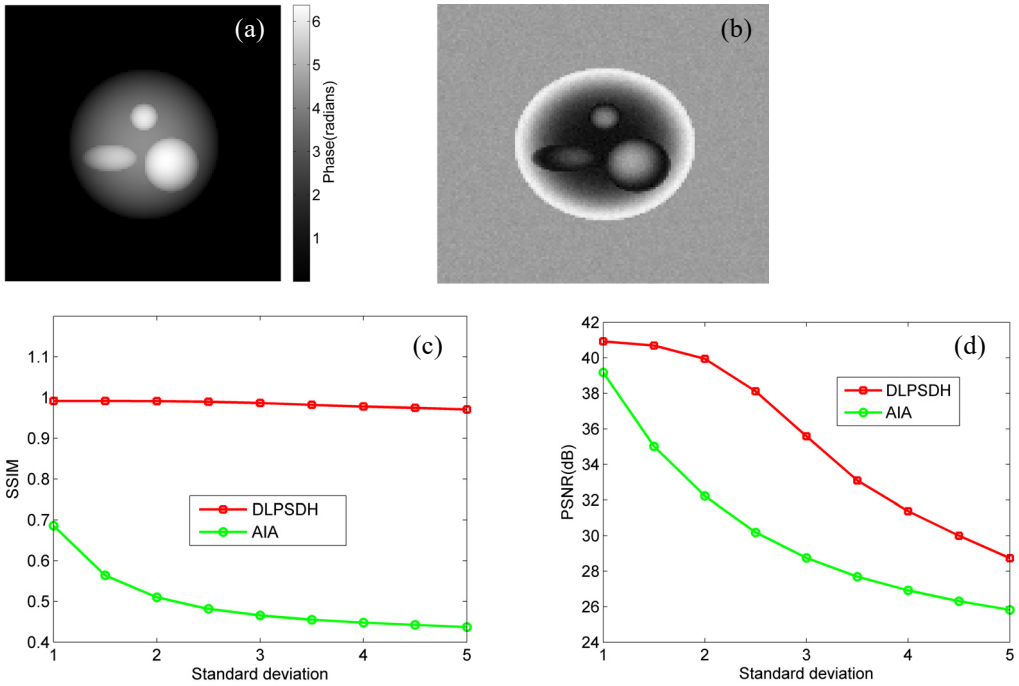

Fig. 5. The neutrophil cell: (a) the original phase, (b) one-frame interferogram, (c) and (d) the values of SSIM and PSNR corresponding to different standard deviations of zero-mean Gaussian noise, respectively, with the DLPSDH and AIA methods.

constants, respectively. The phases of the noisy neutrophil cell are extracted using the proposed and AIA methods, and then the values of SSIM and PSNR of the phase images are shown in Figs. 5(c) and (d), respectively. From Fig. 5(c), we can know that when σ increases from 1 to 5, the values of SSIM decrease in the AIA method; but, the values of SSIM in the proposed method are almost unchanging. From Fig. 5(d), we can know that with the increase of standard deviations, the values of PSNR decrease in the proposed and AIA methods. We can conclude that the SSIMs and PSNRs of the phase images with the DLPSDH method have better values, compared with the AIA algorithm. The DLPSDH method has better anti-noise performance in QPI of the neutrophil cell.

Thirdly, according to Eq. (12), the original phase of the basophil cell is shown in Fig. 6(a). To compare the accuracy of phase retrieval, the interferogram with 7 rad phase shift for the basophil cell, as shown in Fig. 6(b), is used to retrieve the phase with different methods. We present the phases obtained with the DLPSDH, AIA and FSPS methods in Figs. 6(c), (d) and (e), respectively. To test the performance of the DLPSDH method, the horizontal sections of the original and calculated height images of the basophil cell in the horizontal row are depicted in Fig. 6(f). Through the calculation, the RMSEs of the basophil cell with the DLPSDH method, AIA and FSPS methods, respectively, are 0.033, 0.093 and 0.094 rad. From Fig. 6(f), the calculated height

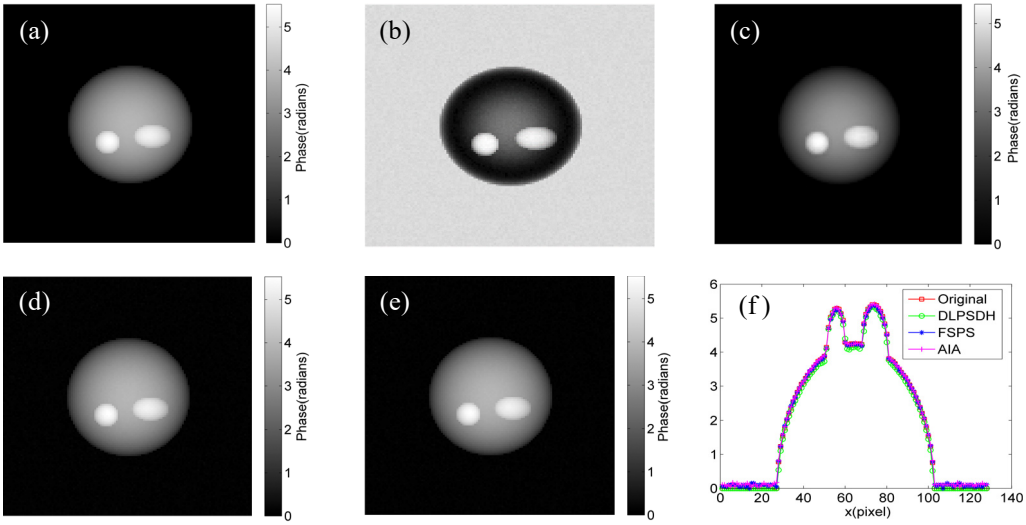

Fig. 6. The basophil cell: (a) the original phase, (b) one-frame interferogram, (c), (d), (e) the extracted phases with the DLPSDH, AIA and FSPS methods, and (f) the horizontal sections of (a), (c), (d) and (e).

curves almost agree with the original height curve, showing the applicability of the proposed method for QPI of the basophil cell.

Finally, in the presence of random phase shifts, we also study the phase extraction of the lymphocyte cell and eosinophil cell, respectively, according to Eqs. (10) and (13). For the eosinophil cell, its RMSEs with the DLPSDH method, AIA and FSPS methods, respectively, are 0.075, 0.087 and 0.107 rad; for the lymphocyte cell, its RMSEs with the DLPSDH method, AIA and FSPS methods respectively are 0.091, 0.226 and 0.227 rad. Note that these interferograms in the testing dataset are different from those in the training dataset. The results above show that the DLPSDH method can recover the phase for different types of WBCs as long as it can establish the continuous mapping function relation of the interferogram to the phase, revealing better generalization performance.

6. Conclusions

In summary, we have proposed an end-to-end deep-learning phase-shifting digital holography method to simultaneously deal with the problems of phase retrieval and phase unwrapping. With a well-trained deep convolutional neural network, this method can establish the continuous function mapping relation between the interferogram and the phase. The proposed method can directly retrieve the phase of white blood cells from only one-frame phase-shifted interferogram, without phase unwrapping operation. Compared with other traditional phase demodulation methods, the proposed method has better phase retrieval accuracy. Simulation experiments demonstrate the feasibility and applicability of the proposed method. Additionally, owing to easily re-

training the well-trained deep neural network using new dataset, this method will provide a solution for phase imaging of biological cells with complex substructures.

Acknowledgements
This work was supported by Changzhou Sci&Tech Program (Grant No. CJ20210032), and by the cultivation object of major scientific research project in Changzhou Vocational Institute of Mechatronic Technology (No. 2020ZDXM003).

References

[1] Yaqoob Z., Psaltis D., Feld S., Yang C., *Optical phase conjugation for turbidity suppression in biological samples*, Nature Photonics **2**(2), 2008: 110–115, DOI: 10.1038/nphoton.2007.297.
[2] Xu X., Wang Y., Ji Y., Xu Y., Xie M., Han H., *A novel dual-wavelength iterative method for generalized dual-wavelength phase-shifting interferometry with second-order harmonics*, Optics and Lasers in Engineering **106**, 2018: 39–46, DOI: 10.1016/j.optlaseng.2018.02.007.
[3] Xu X., Wang Y., Xu Y., Jin W., *Simultaneous measurement of refractive index and thickness for optically transparent object with a dual-wavelength quantitative technique*, Optica Applicata **46**(4), 2016: 597–605, DOI: 10.5277/oa160407.
[4] Bhaduri B., Popescu G., *Derivative method for phase retrieval in off-axis quantitative phase imaging*, Optics Letters **37**(11), 2012: 1868–1870, DOI: 10.1364/OL.37.001868.
[5] Popescu G., *Quantitative Phase Imaging of Cells and Tissues*, McGraw-Hill, 2011.
[6] Vargas J., Quiroga J.A., Sorzano C.O.S., Estrada J.C., Carazo J.M., *Two-step demodulation based on the Gram–Schmidt orthonormalization method*, Optics Letters **37**(3), 2012: 443–445, DOI: 10.1364/OL.37.000443.
[7] Yamaguchi I., Zhang T., *Phase shifting digital holography*, Optics Letters **22**(16), 1997: 1268–1270, DOI: 10.1364/OL.22.001268.
[8] Wang Z., Han B., *Advanced iterative algorithm for phase extraction of randomly phase-shifted interferograms*, Optics Letters **29**(14), 2004: 1671–1673, DOI: 10.1364/OL.29.001671.
[9] Kemper B., von Bally G., *Digital holographic microscopy for live cell applications and technical inspection*, Applied Optics **47**(4), 2008: A52–A61, DOI: 10.1364/AO.47.000A52.
[10] Zhao M., Huang L., Zhang Q., Su X., Asundi A., Kemao Q., *Quality-guided phase unwrapping technique: comparison of quality maps and guiding strategies*, Applied Optics **50**(33), 2011: 6214–6224, DOI: 10.1364/AO.50.006214.
[11] Lo C.F., Peng X., Cai L., *Surface normal guided method for two-dimensional phase unwrapping*, Optik **113**(9), 2002: 439–447, DOI: 10.1078/0030-4026-00183.
[12] Gass J., Dakoff A., Kim M.K., *Phase imaging without 2π ambiguity by multiwavelength digital holography*, Optics Letters **28**(13), 2003: 1141–1143, DOI: 10.1364/OL.28.001141.
[13] Wagner C., Osten W., Seebacher S., *Direct shape measurement by digital wavefront reconstruction and multi-wavelength contouring*, Optical Engineering **39**(1), 2000: 79–85, DOI: 10.1117/1.602338.
[14] Qiu X., Zhong L., Xiong J., Zhou Y., Tian J., Li D., Lu X., *Phase retrieval based on temporal and spatial hybrid matching in simultaneous phase-shifting dual-wavelength interferometry*, Optics Express **24**(12), 2016: 12776–12787, DOI: 10.1364/OE.24.012776.
[15] Cybenko G., *Approximation by superpositions of a sigmoidal function*, Mathematics of Control, Signals, and Systems **2**(4), 1989: 303–314, DOI: 10.1007/BF02551274.
[16] LeCun Y., Bengio Y., Hinton G., *Deep learning*, Nature **521**, 2015: 436–444, DOI: 10.1038/nature14539.
[17] Nguyen T., Bui V., Lam V., Raub C.B., Chang L.C., Nehmetallah G., *Automatic phase aberration compensation for digital holographic microscopy based on deep learning background detection*, Optics Express **25**(13), 2017: 15043–15057, DOI: 10.1364/OE.25.015043.

[18] WU Y., RIVENSON Y., ZHANG Y., WEI Z., GUNAYDIN H., LIN X., OZCAN A., *Extended depth-of-field in holographic imaging using deep-learning-based autofocusing and phase recovery*, Optica **5**(6), 2018: 704–710, DOI: 10.1364/OPTICA.5.000704.

[19] SHIMOBABA T., TAKAHASHI T., YAMAMOTO Y., ENDO Y., SHIRAKI A., NISHITSUJI T., HOSHIKAWA N., KAKUE T., ITO T., *Digital holographic particle volume reconstruction using a deep neural network*, Applied Optics **58**(8), 2019: 1900–1906, DOI: 10.1364/AO.58.001900.

[20] ZHANG G., GUAN T., SHEN Z., WANG X., HU T., WANG D., HE Y., XIE N., *Fast phase retrieval in off-axis digital holographic microscopy through deep learning*, Optics Express **26**(15), 2018: 19388–19405, DOI: 10.1364/OE.26.019388.

[21] RIVENSON Y., ZHANG Y., GUNAYDIN H., TENG D., OZCAN A., *Phase recovery and holographic image reconstruction using deep learning in neural networks*, Light: Science & Applications **7**, 2018: 17141–17149, DOI: 10.1038/lsa.2017.141.

[22] WANG H., LYU M., SITU G., *eHoloNet: a learning-based end-to-end approach for in-line digital holographic reconstruction*, Optics Express **26**(18), 2018: 22603–22614, DOI: 10.1364/OE.26.022603.

[23] WANG K., LI Y., KEMAO Q., DI J., ZHAO J., *One-step robust deep learning phase unwrapping*, Optics Express **27**(10), 2019: 15100–15115, DOI: 10.1364/OE.27.015100.

[24] XU X., XIE M., JI Y., WANG Y., *Dual-wavelength interferogram decoupling method for three-frame generalized dual-wavelength phase-shifting interferometry based on deep learning*, Journal of the Optical Society of America A **38**(3), 2021: 321–327, DOI: 10.1364/JOSAA.412433.

[25] XU X., XIE M., CHEN S., JI Y., WANG Y., *Interferogram blind denoising using deep residual learning for phase-shifting interferometry*, Optica Applicata **52**(1), 2022: 101–116, DOI: 10.37190/oa220108.

[26] FALK T., MAI D., BENSCH R., CICEK O., ABDULKADIR A., MARRAKCHI Y., BOHM A., DEUBNER J., JACKEL Z., SEIWALD K., DOVZHENKO A., TIETZ O.I., BOSCO C. D., WALSH S., SALTUKOGLU D., TAY T.L., PRINZ M., PALME K., SIMONS M., DIESTER I., BROX T., RONNEBERGER O., *U-Net: deep learning for cell counting, detection, and morphometry*, Nature Methods **16**, 2019: 67–70, DOI: 10.1038/s41592-018-0261-2.

[27] KINGMA D.P., BA J., *Adam: A method for stochastic optimization*, 2017, http://arxiv.org/abs/1412.6980.

[28] WANG Z., BOVIK A.C., SHEIKH H.R., SIMONCELLI E.P., *Image quality assessment: from error visibility to structural similarity*, IEEE Transactions on Image Processing **13**(4), 2004: 600–612, DOI: 10.1109/TIP.2003.819861.

Received April 11, 2022
in revised form July 20, 2022